Applied Catalysis B: Environment and Energy 344 (2024) 123633

Contents lists available at ScienceDirect

Applied Catalysis B: Environment and Energy

journal homepage: www.elsevier.com/locate/apcatb

High-efficiency electrochemical methane conversion using Fe_2O_3-based catalysts assisted by thermochemical active oxygen

Jaehyun Lee [c,1], Sungwoo Lee [b,1], Cheolho Kim [a], Jong Suk Yoo [b,*], Jun Hyuk Moon [a,*]

[a] Department of Chemical and Biological Engineering, Korea University, Seoul 02841, Republic of Korea
[b] Department of Chemical Engineering, University of Seoul, Seoul 02504, Republic of Korea
[c] Department of Chemical and Biomolecular Engineering, Sogang University, Seoul 04107, Republic of Korea

ARTICLE INFO

Keywords:
Electrochemical methane oxidation
Thermochemical oxygen generation
Zirconium doping
Methane-ethanol conversion

ABSTRACT

Direct methane-alcohol conversion is urgently needed not only for efficient use of methane but also for a sustainable environment. Here, we present hybrid electrochemical methane oxidation with thermochemical generation of active oxygen by employing an Fe_2O_3-based catalyst with a CO_3^{2-} oxygen source. A mechanistic study, including an electrochemical analysis, elucidates the reaction pathway in which the CO_3^{2-} activates methane by supplying O* through thermal dissociation over the Fe_2O_3 catalyst, while an electrochemical potential applied to the Fe_2O_3 catalyst promotes the subsequent methane–ethanol conversion. We demonstrate that doping the catalyst with oxophilic Zr into the catalyst enhances ethanol conversion by stabilizing the hydroxyl-containing intermediates. In room-temperature electrochemical methane conversion, we achieve an ethanol production rate of 1677 μmol/g_{cat}/hr (the total production rate for oxygenates is 1831 μmol/g_{cat}/hr) with a selectivity of 91 % and an 87 % Faraday efficiency conversion.

1. Introduction

The demand for conversion of methane into high value-added chemicals is surging with the abundant supply from shale gas development [1,2]. Conversion of methane to alcohol is advantageous not only in terms of storage/transportation but also in that alcohol can be directly used as a liquid fuel [3]. Since direct conversion of methane to alcohol is difficult due to the high C–H binding energy of methane (439 kJ/mol) with low electron affinity [4–7], commercialized methane-alcohol conversion adopts the route of first decomposing methane (high-temperature reforming, typically >1100 K) at high temperature to produce syngas and then synthesizing alcohol through multistep indirect conversion [8–10]. However, the multistep conversion process including such high-temperature reforming always suffers from economic issues [8–10]. Therefore, for direct methane-alcohol conversion, advanced thermochemical catalysts such as Fe- or Cu-based zeolites (e.g., Fe-ZSM-5, FeCu-ZSM-5, Cu-mordenite) have been extensively explored [11,12]. Specifically, these catalysts mimic the metal-oxo active site of methane monooxygenase that converts methane to methanol at room temperature [13]. Nevertheless, the catalytic process still adopts a multistep process with varying temperature [14,15]. The process typically consists of activation of the metal-zeolite catalyst by an oxidant (473–773 K), methane oxidation on the metal-oxo site of the catalyst (398–473 K), and extraction of methanol with steam/solvent (473 K). Recently, continuous methane-methanol conversion at a constant temperature over a Cu-zeolite catalyst has been demonstrated, but the conversion rate is extremely low, 0.001 % [16].

Electrocatalytic liquid-phase methane conversion is emerging as a continuous multistep methane–alcohol direct conversion process under mild conditions [17,18]. Specifically, electrocatalytic conversion exhibits distinct features for each step of a catalytic process: catalyst activation, methane oxidation, and product extraction. First, catalyst activation, which is the formation of active atomic oxygen on the catalyst surface, is continuously achieved by electrochemically oxidizing water ($H_2O \rightarrow OH^* \rightarrow O^*$); this process overlaps with the oxygen evolution reaction (OER) [19,20]. Then, catalytic conversion is controlled by simply adjusting the applied potential [21]. Finally, the electrolyte solution environment allows the immediate extraction of highly soluble alcohol products and the consequent suppression of deep oxidation processes [22,23]. Previously, Singh and coworkers suggested high electrochemical methane oxidation in transition metal oxides such as TiO_2 with high methane binding energy induced by a low Madelung

* Corresponding authors.
E-mail addresses: jsyoo84@uos.ac.kr (J.S. Yoo), junhyukmoon@korea.ac.kr (J.H. Moon).
[1] These authors equally contributed to this work.

https://doi.org/10.1016/j.apcatb.2023.123633
Received 30 April 2023; Received in revised form 10 December 2023; Accepted 13 December 2023
Available online 16 December 2023
0926-3373/

potential [24]. Zheng and coworkers performed room temperature electrochemical methane–ethanol conversion with an ethanol production rate of 789 μmol/g_{cat}/hr (85 % selectivity) on a Rh/ZnO nanosheet catalyst [25]. Sun and coworkers demonstrated electrochemical methane–ethanol conversion over NiO/Ni catalysts with a production rate of 25 μmol/g_{cat}/hr (87 % selectivity) [26]. Nevertheless, the benefits of electrocatalysis have not been fully realized. The biggest hurdle is that the formation of stable O* is difficult under anodic potential as O* is prone to being scavenged by the OER [24]; this issue also occurs with the introduction of a separate oxidant. Besides, highly active methane oxidation catalysts are characterized by weak oxygen binding, so they are likely to exhibit fast OERs [17,19]. Indeed, previous studies on electrochemical methane oxidation with a bimetallic Cu_2O_3/TiO_2 catalyst and a Mg-MOF-74 catalyst reported low Faraday efficiencies (FEs) of 6 % and 10.9 %, respectively, which may be associated with fast OERs [24,27]. Therefore, exploring electrocatalytic reactions with stable O* formation is pursued for highly productive electrochemical methane conversion.

In this study, we present electrochemical methane–ethanol conversion using an Fe_2O_3-based catalyst with a CO_3^{2-} oxygen source (Fig. 1a). Although Fe_2O_3 is applicable as a catalyst for the thermochemically complete oxidation of methane and as a photoelectrochemical water splitting catalyst [28,29], it has yet to be applied to electrochemical methane conversion processes. The CO_3^{2-} oxygen source has been utilized; however, the usefulness of CO_3^{2-} has not been fully elucidated through mechanistic analysis [30,31]. In this study, our density functional theory (DFT) calculations and experiments reveal that the generation of O* by the dissociative adsorption of CO_3^{2-} on the Fe_2O_3 catalyst occurs thermochemically, avoiding the OER. In addition, we identify a favorable reaction pathway for methane–ethanol conversion; this solution involves a methanol deprotonation process that becomes more endothermic under anodic potentials. Furthermore, we present the promotion of methane–ethanol conversion by Zr doping. Under room-temperature electrochemical methane conversion conditions, we achieve highly selective methane–ethanol conversion with Fe_2O_3-based catalysts. The Zr-doped Fe_2O_3 catalyst attains an ethanol production rate of 1677 μmol/g_{cat}/hr ((the total production rate for oxygenates is 1831 μmol/g_{cat}/hr) with a selectivity reaching 91 %; the Faraday efficiency (FE) for this ethanol conversion process approaches 87 %. This value exceeds the production rate for the partial oxidation of methane resulting from existing electrocatalysts, photocatalysts and liquid-phase heterogeneous catalysts.

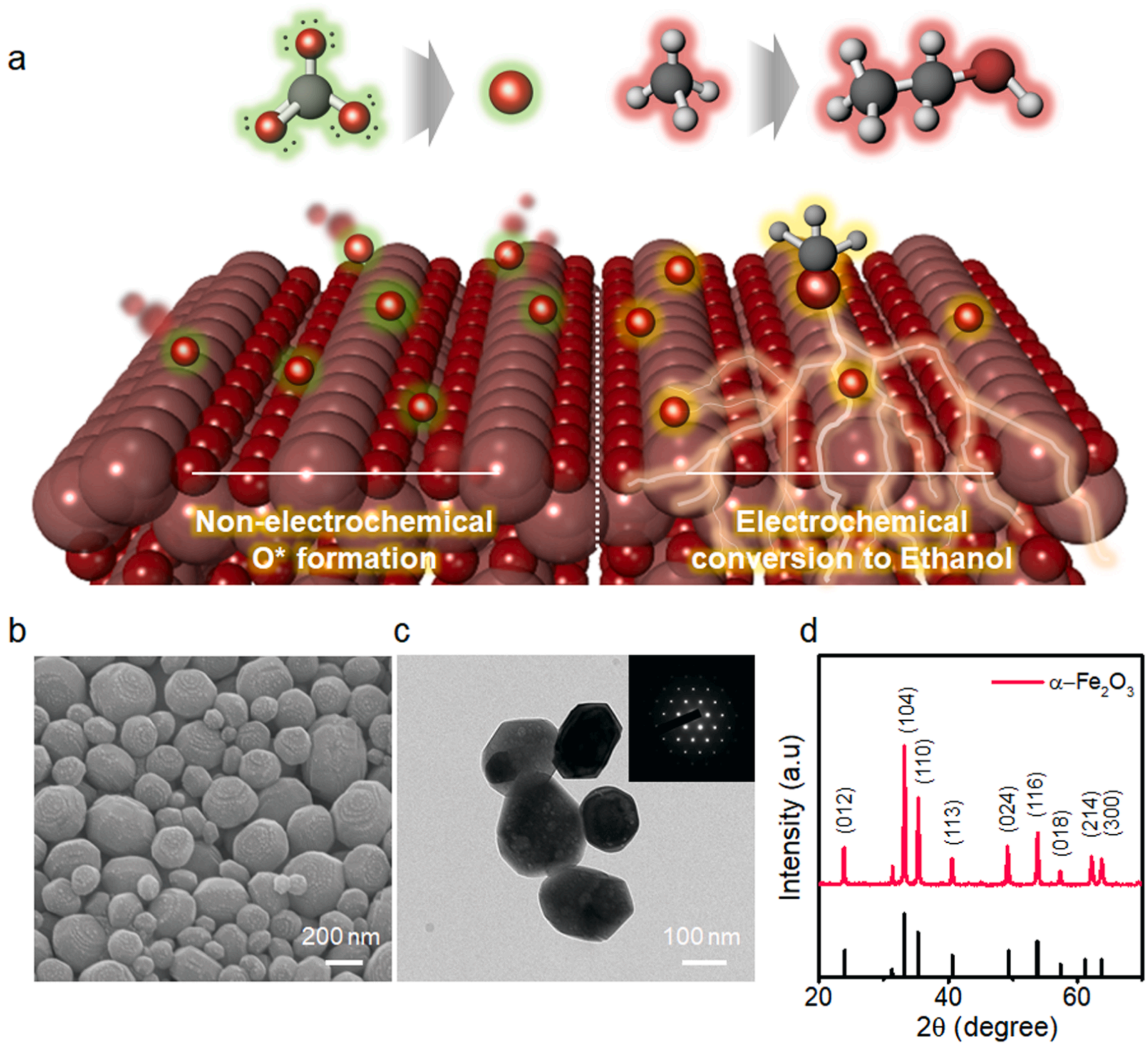

Fig. 1. Material analysis of the Fe_2O_3 catalyst. (a) Schematic diagram of electrochemical oxidation of methane to ethanol assisted by thermochemical generation of active oxygen. (b) Scanning electron microscopy (SEM) and (c) transmission electron microscopy (TEM) images of Fe_2O_3 catalyst nanoparticles. The inset image is the SAED pattern. (d) XRD pattern of the Fe_2O_3 catalyst. (Reference: JCPDS 33 – 0664 for α-Fe_2O_3.).

2. Experimental

2.1. Preparation of α-Fe_2O_3 catalyst

The α-Fe_2O_3 catalyst was obtained by reacting 0.03 M Iron(III) nitrate nonahydrate and 0.06 M NaCl and 0.2 g poly(N-vinylpyrrolidone) (K-30) were dissolved in mixed solvents of 15 mL DI water and 15 mL ethanol under magnetic stirring. For zirconium doping, calculated amount of Zirconium(IV) oxynitrate hydrate was added to the previously prepared mixed solution to obtain the 0.01, 0.05 and 0.1 wt % Zr-doped Fe_2O_3. The mixed solution was loaded into a 100 mL Teflon autoclave sealed to 433 K and kept at this temperature for 12 h. The synthesized particles were thoroughly washed with ethanol. Thereafter, the particle was heat treated at 1073 K for 6 h.

2.2. Electrochemical analysis and methane-conversion reaction

The measurement of current versus voltage sweep utilizes a three-electrode system exploiting α-Fe_2O_3 catalyst-coated glassy carbon as the working electrode, Pt as the counter electrode, and a saturated calomel electrode (SCE) as the reference electrode, using a potentiostat (was recorded using a Versastat, Ametek); The scan rate was 0.02 V/s. The electrolyte contains 0.5 M Na_2CO_3, where the Na_2CO_3 acts as an oxidizing agent. The dissolution of methane in the electrolyte is obtained by purging the electrolyte with methane at a rate of 30 mL/min for about 30 min before the reaction. The α-Fe_2O_3 catalyst coated on graphite foil were applied as catalyst electrodes; The coating is obtained by casting a solution of the particles dispersed in Nafion-dissolved ethanol solution (1 % (v/v)) followed by drying in an oven at 373 K for 24 h. The conversion reaction is carried out in a gas-tight reactor (450 mL); The area of the catalyst electrode is typically 10 cm^2. An electrolyte of 0.5 M Na_2CO_3 is applied. For isotopically-labeled reactions, $^{13}CH_4$ was purchased from Sigma-Aldrich (99 %, 99 atom % ^{13}C). ^{18}O-labeled carbonate was synthesized by reacting $H_2^{18}O$ (200 μL, 9.1 mmol, 98 % ^{18}O) with tetraethyl orthocarbonate (5 mL, 23.8 mmol) and toluenesulfonic acid (dehydrated, 1.5 mg) for several minutes. It was then dried and reacted with 500 mM sodium methoxide solution (at 385 K for 30 hrs).

2.3. Characterization

The scanning electron microscope (SEM) was recorded using a JSM-7800F (JEOL). The transmission electron microscope (TEM) was recorded using a JEM-ARM200F (JEOL); The microscope was equipped with a spherical aberration corrector in the condenser lens (probe corrector). The high-angle annular dark field-scanning TEM (HAADF-STEM) was conducted by using a JEM-ARM200F (JEOL) microscope at an acceleration voltage of 200 kV. The EDS mapping was recorded using Oxford Instruments X-Max SDD. The XRD was recorded using a Rigaku miniflex-2005G303 X-ray diffractometer (Cu Kα radiation at 20 kV and 10 mA) in the 2 theta range of 20–70°. The XPS was analyzed by using a Leybold photoelectron spectroscopy (Al Ka monochromatic beam). ^{13}C NMR is recorded using an Avance III HD 400 FT NMR instrument (Bruker Biospin). The measurement is calibrated with a signal of 3-(trimethylsilyl)–1-propane sulfonic acid sodium salt (DSS) at $\delta = 0.0$ ppm. The proton high-power decoupling field strength was 11.7 G (5.0 μs long 90° ^{1}H pulses). The contact time was 4 ms at the Hartmann-Hahn matching condition 50 kHz, and the scan delay time was 3 s. The ^{13}C chemical shift of the product was analyzed for accuracy of ±0.5 ppm. Tetramethylsilane (TMS) was applied as an external standard. The ^{13}C chemical shift of the product was analyzed with an accuracy of ± 0.5 ppm; Tetramethylsilane (TMS) was applied as an external standard.Gas chromatography (GC) was obtained using gas chromatography (7820 A, Agilent Technologies, USA) using a flame ionization detector (FID). A PoraPLOT Q column was used, the samples were injected with an airtight syringe, and the injection temperature was 523 K. For the FID a flow of 300 mL/min Ar, 40 mL/min H_2 fuel and 25 mL/min N_2 make-up was applied. Oven temperature conditions are 2 min at 313 K, 353 K (20 K/min) and 503 K (30 K/min). Gas chromatography-mass spectra are measured by gas chromatography (GC-MS, 7890B-5977A, Agilent Technologies, USA) equipped with a mass selective detector MSD 5975 (electron impact ionization, EI, 70 eV, Agilent Technologies). Fused silica capillaries (DB-WAX, 0.5 μm thick poly(ethylene glycol) coating, Agilent Technologies, USA) are utilized. The injection temperature is 250 degrees. The carrier gas is helium (1 mL/min, 99.999 %) and the dilution ratio is 10:1 (sample: He). Oven temperature conditions are 5 min at 313 K, 4 K/min (373 K), and 3 min at 513 K (20 K/min).

3. Results and discussion

3.1. Catalyst synthesis

Fe_2O_3 nanoparticles are synthesized by the hydrothermal reduction of an iron(III) nitrate precursor[32]. The Fe_2O_3 particles have polyhedral shapes with diameters in the range of 50–300 nm (Fig. 1b and S1). The Brunauer–Emmett–Teller (BET) surface area is 176 m^2/g (Fig. S2). The selected area electron diffraction (SAED) pattern shows sharp diffraction spots, indicating high crystallization (Fig. 1c). The X-ray diffraction (XRD) pattern exhibits peaks corresponding to α-Fe_2O_3 (JCPDS 33–0664) (Fig. 1d).

3.2. Comparison of O* formation from water vs. CO_3^{2-} on the Fe_2O_3 catalyst

DFT calculations are employed to compare O* formation from water vs. CO_3^{2-} on Fe_2O_3. We employ an α-Fe_2O_3 (0001) facet, which is considered an active surface in various electrochemical oxidation reactions [33–35]. We confirm that α-Fe_2O_3 is the most stable phase under our experimental conditions (pH = 10–12, applied voltage of ~0.8 V vs. saturated calomel electrode (SCE) (V_{SCE})) based on a bulk Pourbaix diagram analysis [36,37].

The calculated free energy profile for the formation of O* from water via the OER is presented in Fig. 2a. Among all the oxygen intermediates, i.e., OH*, O* and OOH*, we consider O* the active oxygen species for methane activation since the activation barrier for the OH*-assisted route (1.2 eV) is approximately twice as high as that for the O*-assisted route (0.6 eV). Notably, the OH* → O* step is the potential determining step, indicating that we cannot create O* on α-Fe_2O_3 (0001) via OER[38]. Applying the limiting potential of 2.0 V_{RHE} to promote the OH* → O* step makes the whole OER process exothermic; thus, the system rapidly generates O_2, as shown in Fig. S3. The fast OER on α-Fe_2O_3 (0001) indicates the poor utilization of O* for methane activation. External oxidants inevitably generate O* on α-Fe_2O_3 (0001) during the electrochemical methane conversion process.

The calculated free energy profile for the formation of O* from CO_3^{2-} is presented in Fig. 2b. Since it is difficult to directly calculate the energy of CO_3^{2-} solvated by water, we employ a thermodynamic cycle method (supplementary note #2) to indirectly obtain the energy. The electrochemical adsorption of CO_3^{2-} ($CO_3^{2-} \rightarrow CO_3^* + 2e^-$) is endothermic by 1.6 eV. However, if we assume that CO_3^{2-} adsorption involves nearly a two-electron transfer reaction, the process becomes thermoneutral at 0.8 V_{RHE}. Under our experimental conditions for methane oxidation, i.e., 0.8 V_{SCE}, which is approximately 1.6 V_{RHE}, CO_3^{2-} adsorption becomes exothermic by 0.8 eV. Once CO_3* forms, it thermodynamically decomposes to O* and CO_2 with a surmountable activation barrier of 0.8 eV. Notably, our experimental condition of 1.6 V_{RHE} for methane activation falls short of completely promoting the OER, in which the limiting potential is 2.0 V_{RHE}. This finding suggests that O* that forms from CO_3^{2-} does not oxidize to OOH* and then O_2 gas; instead, it is utilized for O*-assisted methane activation, as shown in Fig. 2a.

The formation of O* from CO_3^{2-} on the Fe_2O_3 surface is confirmed experimentally. We analyze the gaseous product by applying an anodic

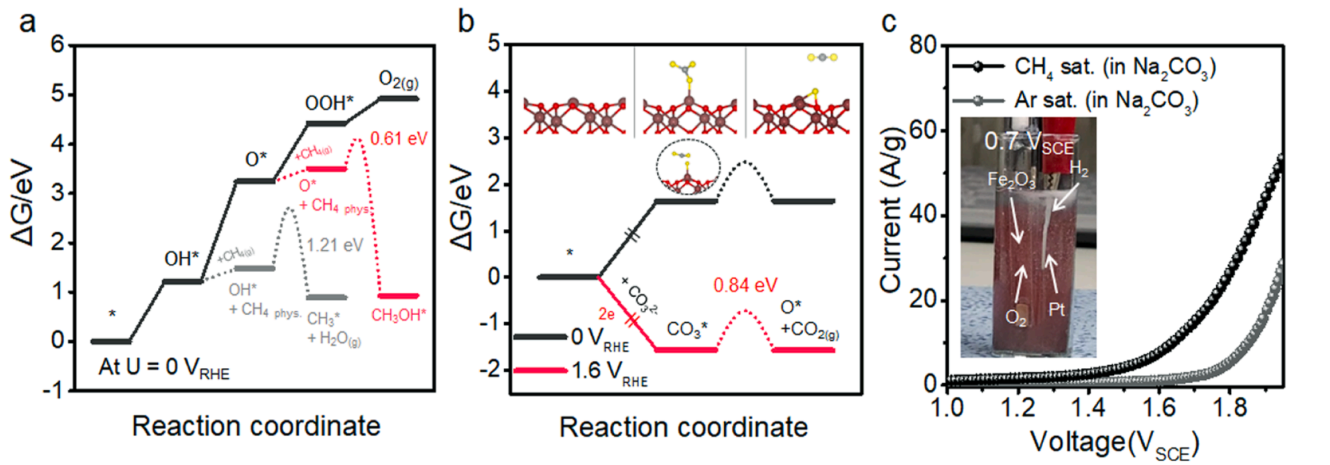

Fig. 2. DFT and LSV studies. (a) Free energy diagram for the OER on the Fe_2O_3 catalyst. Methane oxidation by O*–assisted (red) and OH*–assisted (gray) pathways are also displayed. (b) Free energy diagram for adsorption dissociation of CO_3^{2-} at potentials of 0 V_{RHE} and 0.8 V_{RHE}. The inset presents the atomic configuration for each reaction coordinate. The dark red, red/yellow, and gray spheres represent Fe, O, and C, respectively. The solid and dotted lines represent the electrochemical and thermodynamic routes, respectively. (c) LSV curves of Fe_2O_3 in CH_4-saturated and Ar-saturated electrolytes (control). (inset) Digital camera image of the three-electrode reactor at 1.6 V_{RHE}.

potential of 1.6 V_{RHE} to the Fe_2O_3 catalyst electrode in a methane-saturated CO_3^{2-} electrolyte. In situ mass spectrometry detects CO_2 (g) (Fig. S4); this CO_2 is released by the thermochemical dissociation of CO_3*(CO_3* → CO_2 (g) + O*), confirming the formation of O*. The O 1s X-ray photoelectron spectroscopy (XPS) spectrum of the potential-applied Fe_2O_3 catalyst surface is presented (Fig. S5). The spectrum shows a high-intensity peak for the surface oxygen, confirming the presence of O*[39,40].

Additionally, we analyze the linear sweep voltammetry (LSV) profile of the Fe_2O_3 catalyst in the electrolyte (Fig. 2c). The LSV curve exhibits a rapidly increasing oxidation current with an onset potential of approximately 1.6 V_{RHE}. This oxidation current is caused by water splitting; we observe the vigorous evolution of O_2 (g) and H_2 (g) on Fe_2O_3 and Pt electrode surfaces, respectively, at 2.4 V_{RHE} (Fig. S6). The LSV curve in the methane-saturated electrolyte exhibits a distinct profile from that in the bare electrolyte. The onset potential for the oxidation current exceeds the previous value of 1.0 V_{RHE}. This result reveals that methane oxidation proceeds prior to the OER on Fe_2O_3; at 1.6 V_{RHE}, little gas evolves at the Fe_2O_3 electrode, despite the evolution of H_2 at the Pt electrode (Fig. 2c); this phenomenon shows the production of water-soluble products (later identified as ethanol) by methane oxidation at the Fe_2O_3 electrode. The LSV analysis confirms a continuous production of stable O* that drives the conversion of methane rather than the evolution into O_2.

3.3. *Analysis of methane oxidation products and reaction pathways*

We employ isotopically labeled CH_4 ($^{13}CH_4$) and CO_3^{2-} ($C^{18}O_3^{2-}$) to identify products in electrochemical methane conversion on the Fe_2O_3 catalyst. The carbon-13 nuclear magnetic resonance (^{13}C NMR) spectrum for the liquid-phase product is shown in Fig. 3a. We identify ethanol as the major product, and all carbon atoms are labeled ^{13}C; small amounts of methanol and acetone with ^{13}C are identified. The gas chromatography—mass spectrometry (GC—MS) spectrum for ethanol is presented in Fig. 3b. In addition to the peaks assigned to ^{16}O ethanol, we observe peaks shifted by 2 *m/z*, which correspond to ^{18}O-containing ethanol. The intensity of the shifted peak is approximately 40 % of the ^{16}O ethanol peak intensity. This ratio corresponds to the ratio of $C^{16}O_3^{2-}$: $C^{18}O_3^{2-}$ used in the reaction, indicating that there is CO_3^{2-} is the only oxygen source. The isotope reaction identifies the conversion of methane to alcohol by the oxygen from CO_3^{2-}.

The productivities for methane conversion at various applied voltages are compared, as shown in Fig. 3c (Table 1). Under all conditions, ethanol is the main product among oxygenates. Ethanol production increases to 1.6 V_{RHE}. However, at high applied voltages, ethanol production decreases. This phenomenon corresponds to a decrease in methane conversion productivity as O* is consumed in the OER. In the LSV profile, the oxidation current for the OER rapidly increases from 1.6 V_{RHE}. The production rate is the highest at 1.6 V_{RHE}, achieving 1198.3 μmol/g_{cat}/hr with 86 % selectivity; the FE for total oxygenates is 87 %. The maximum production rate surpasses those of previous electrocatalysts, including CuO/CeO_2 (1009.8 μmol/g_{cat}/hr for methanol), Rh/ZnO (789 μmol/g_{cat}/hr) and NiO/Ni (25 μmol/g_{cat}/hr) (see Table S1). The selectivity is the highest at 1.6 V_{RHE}. Based on this voltage, the ethanol selectivity decreases with the production of methanol in the low-voltage region and the production of acetone in the high-voltage region (Fig. 3d).

DFT calculations are employed to identify the minimum free-energy pathway for methane-to-ethanol conversion on O*/Fe_2O_3; the results are shown in Fig. 3e. The pathway starts by activating methane on O* produced via the thermochemical dissociation of carbonate ions that are electrochemically adsorbed on Fe_2O_3. That is, the C–H bond of methane is cleaved while forming a C–O bond to directly produce CH_3OH*(CH_4+ O* → CH_3OH*, ΔG = –2.6 eV with a low free-energy barrier of 0.6 eV). This O*-assisted methane activation route is thermodynamically preferred to that producing CH_3* and OH*(CH_4+ O* → CH_3* + OH*[41], ΔG = –1.6 eV with a low free-energy barrier of 0.6 eV); nevertheless, both reactions are highly exothermic. Then, CH_3OH* deprotonation occurs via the cleavage of the C–H bond to produce CH_2OH*, as the cleavage of the O–H bond to produce CH_3O* is more endothermic by 2 eV [41–43]. Since CH_3OH* deprotonation is an electrochemical reaction (CH_3OH* → CH_2OH*+ H^+ + e^-), it becomes highly exothermic under an applied potential of 1.6 V_{RHE}, surpassing the competition with CH_3OH* desorption to form methanol (CH_3OH* → CH_3OH, ΔG = 0.3 eV). These results are in agreement with the experimental finding that more ethanol is produced than methanol, particularly at high anodic potentials.

Since CH_2OH*, which has a strong polarity of carbonyl oxygen, is susceptible to nucleophilic attacks, direct bonding between CH_2OH* and CH_3* is presumed for ethanol synthesis[44]. Since CH_4 + O*→ CH_3* + OH* is exothermic, CH_3* may form on the catalyst surface. Fig. S7 shows the calculated free energy profile for ethanol production via the coupling of CH_2OH* and CH_3*. While this route seems possible with the highest free energy barrier of approximately 0.8 eV, it leads to

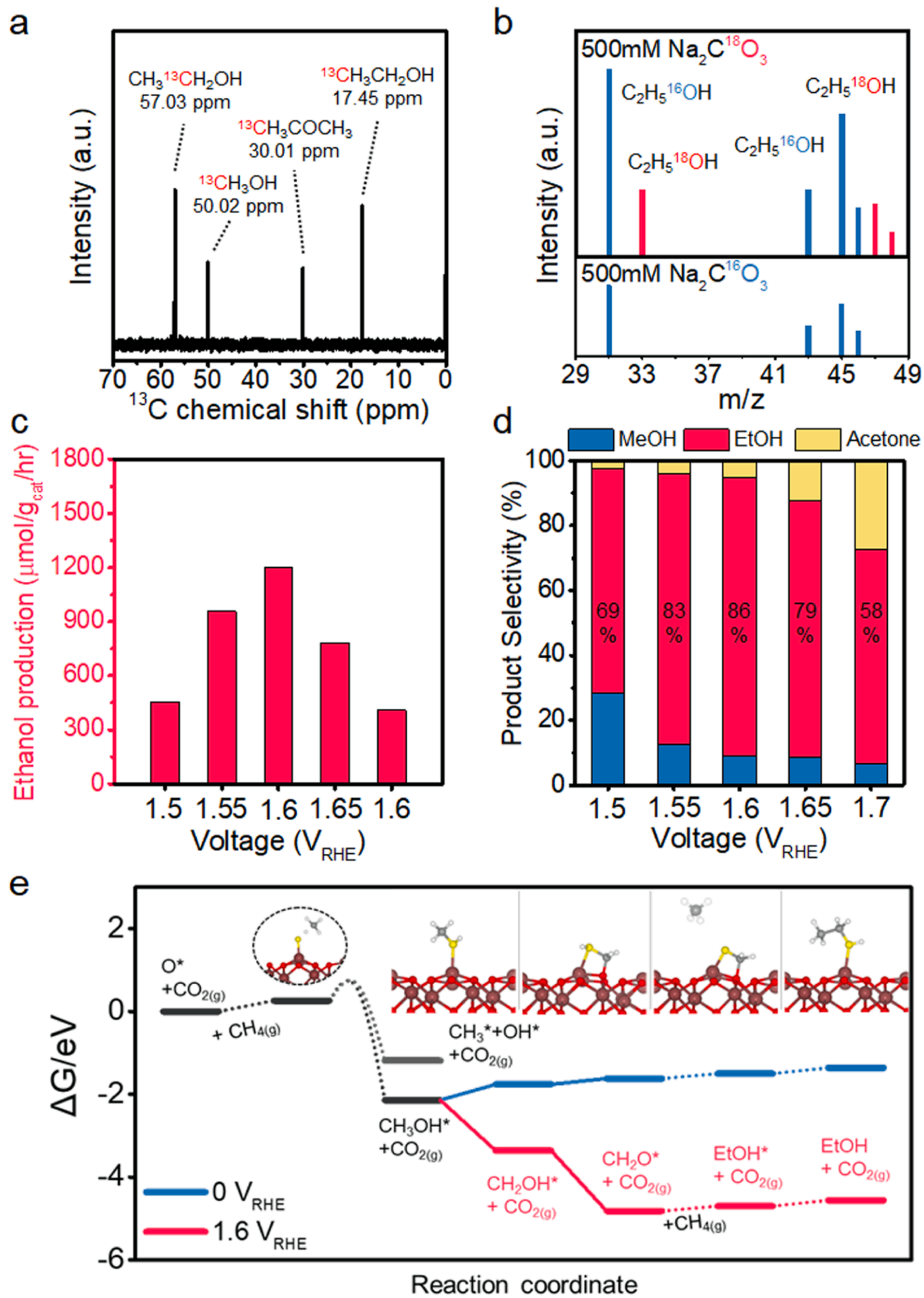

Fig. 3. Electrochemical methane–ethanol conversion. (a) ^{13}C NMR spectrum of the product reacted using $^{13}CH_4$. (b) GC–MS spectrum for ethanol of the product reacted using $C^{18}O_3^{2-}$. (c) Ethanol production at various applied voltages. (d) Selectivity for the main oxygenates at various applied voltages. (e) Calculated free energy diagrams for methane–ethanol conversion at 0 V_{RHE} and 1.6 V_{RHE}. The cartoons are atomic configurations corresponding to each reaction coordinate. The solid and dashed lines represent the electrochemical and thermochemical steps, respectively.

the formation of OH* (CH_4 + O*→ CH_3*+OH*) that is difficult to remove from the catalyst surface via OER. If we apply the limiting potential for the OER (2.0 V_{RHE}) to oxidize OH* to oxygen gas, O* formed from CO_3^{2-} oxidizes to oxygen gas. Thus, ethanol production via the coupling of CH_2OH* and CH_3* is not feasible on α-Fe_2O_3 (0001). CH_2OH* must be further deprotonated to CH_2O*, which is highly exothermic under an applied potential of 1.6 V_{RHE}; then, it must combine with CH_4, as shown in Fig. 3e.

The reaction of CH_2O* with CH_4 to form EtOH* is thermochemical, and the reaction free energy is near thermoneutral; this observation indicates that ethanol production via the coupling of CH_2O* and CH_4 is thermodynamically possible under ambient conditions. The transition state for this reaction step (CH_2O* + CH_4 → EtOH*) resembles a methyl radical interacting with CH_2OH*, in which the energy cannot be calculated accurately, as explicitly modeling the solvation of the methyl radical in water is extremely difficult. However, since no other C–C

Table 1

Comparison of catalytic activity for the liquid phase oxidation of CH_4 using Na_2CO_3. Test condition: catalyst: Fe_2O_3 / Zr-doped Fe_2O_3, Reaction temperature = 298 K, electrolyte = 0.5 M Na_2CO_3, CH_4 pressure = 1 bar, Reaction Time = 1 h.

Entry	Catalyst	Voltage (V_{RHE})	Amount of product (μmol/g_{cat}) (Selectivity)		
			Ethanol	Methanol	Acetone
1	Fe_2O_3	1.5	456 (69.4 %)	185 (28.2 %)	15.3 (2.3 %)
2	Fe_2O_3	1.55	957 (83.5 %)	144 (12.5 %)	45.3 (4.0 %)
3	Fe_2O_3	1.6	1198 (86.1 %)	124 (8.9 %)	70.0 (5.0 %)
4	Fe_2O_3	1.65	783 (79.1 %)	84.6 (8.5 %)	127 (12.4 %)
5	Fe_2O_3	1.7	408 (66.1 %)	40.0 (6.5 %)	169 (27.5 %)
6	0.01 wt% Zr- doped Fe_2O_3	1.6	1369 (88.5 %)	107 (6.9 %)	70.1 (4.5 %)
7	0.05 wt% Zr- doped Fe_2O_3	1.6	1677 (90.5 %)	82.6 (4.3 %)	99.2 (5.2 %)
8	0.1 wt% Zr- doped Fe_2O_3	1.6	1549 (89.8 %)	60.1 (3.5 %)	116 (6.7 %)

bonding routes to form ethanol are possible (once CH_2O^* is further deprotonated to CHO*, there is no pathway to produce ethanol without undergoing reduction (protonation) steps under oxidizing (anodic) conditions in principle), we carefully argue that this is the most feasible route for producing EtOH* on O*/Fe_2O_3. Finally, although the desorption of EtOH* to EtOH (g) is slightly endothermic with a reaction free energy of 0.1 eV, ethanol production in an aqueous environment is likely to be spontaneous; this spontaneity occurs since $EtOH_{(aq)}$ is much lower in energy than EtOH (g) due to hydrogen bonding with the water solvent, and desorption reactions are usually barrierless.

DFT calculations are performed to examine the possibility of the deeper oxidation of ethanol to acetone on the Fe_2O_3 surface. Although the electrochemical barriers are not calculated, ethanol deprotonations occur via EtOH* → CH_3CHOH^* → CH_3CHO^* → CH_3CO^*(Fig. S8). Once CH_3CO^* forms, further deprotonation is extremely endothermic; thus, it reacts with CH_3^* produced via CH_4 + O* → CH_3^*+ OH*(Fig. S9). This CH_3CO^* -CH_3^* coupling reaction directly forms acetone on the surface, in which the desorption is moderately uphill (0.7 eV) in free energy. Although acetone production initially appears to be feasible, for a complete catalytic cycle (stable acetone production), OH* produced via CH_4 + O* → CH_3^*+ OH* must be removed as O_2 via the OER, in which the limiting potential is very high (2.0 V_{RHE}), as discussed above. Even if an anodic potential higher than 2.0 V_{RHE} is applied, acetone production is unlikely to dominate, as O* is oxidized to O_2 and not much O* is available for methane activation. These results are in agreement with the experimental finding that little acetone is produced, particularly at low anodic potentials.

3.4. Improvement of ethanol productivity by Zr doping

Since the key to increasing the ethanol selectivity is to stabilize CH_2OH^* relative to CH_3OH (g), we first theoretically devise a Zr-doping strategy to increase the oxophilicity of the Fe_2O_3 surface to achieve high ethanol selectivity (note that CH_2OH^* binds to the surface through oxygen) [33,45]. Fig. S10 shows the calculated Pourbaix diagram for the Zr-doped α-Fe_2O_3 (0001) surface. Unlike the pristine Fe_2O_3 surface, OH* is strongly preadsorbed on the Zr site of the Zr-doped Fe_2O_3 surface even under weakly oxidizing conditions. Fig. 4a shows the changes in the free energy diagram for the methane to ethanol conversion when Zr is doped to the α-Fe_2O_3 (0001) surface and OH* is preadsorbed on the Zr site. Only the intermediates containing -OH groups, such as CH_3OH^*, CH_2OH^* and EtOH*, are stabilized by 0.1 eV, thermodynamically promoting the ethanol production pathway over methanol. The selective stabilization is attributed to the formation of the hydrogen bond between the -OH group of the intermediate and the preadsorbed OH* (Fig. S11)[46]. Notably, the RPBE functional is used for all these calculations. By using a functional that accurately accounts for dispersion interactions, greater extents of stabilization are to be expected [47,48].

To experimentally verify the strategy for improving the ethanol selectivity, we prepare a Zr-doped Fe_2O_3 catalyst by coprecipitation with a precursor of zirconium(IV) oxynitrate. We control the concentration of the Zr precursor to obtain Fe_2O_3 catalysts containing 0.01, 0.05 and 0.1 wt% Zr. The Zr-doped Fe_2O_3 particles exhibit sizes of 50–300 nm, similar to those of conventional Fe_2O_3 particles (Fig. 4b). The elemental analysis shows a uniform distribution of Zr (Fig. 4c and Fig. S12). The XRD peaks of Zr-doped Fe_2O_3 are similar to those of Fe_2O_3. However, the peaks of Zr-doped Fe_2O_3 are shifted to smaller angles than the peaks of bare Fe_2O_3; this shift is attributed to the expansion of the crystal lattice induced by the incorporation of Zr, in which the atomic radius is approximately twice that of Fe. The peaks corresponding to ZrO_2 are not observed (Fig. 4d).

The ethanol productivity and selectivity on the Fe_2O_3 catalysts with various Zr contents are presented in Figs. 4e and 4f, respectively (Table 1). We achieve the maximum production rate at 0.05 wt% Zr. The low production rate at 0.1 wt% Zr is rationalized by a decrease in conductivity due to lattice distortion caused by Zr doping. Electrochemical impedance spectroscopy is applied to compare the charge transfer resistivity at various doping contents; the lowest resistivity appears at 0.05 wt%, and the resistivity increases at 0.1 wt% (Fig. S13). The ethanol production rate reaches 1677 μmol/g_{cat}/hr at 1.6 V_{RHE}, which is a 53 % improvement compared to the bare Fe_2O_3 catalyst. The ethanol productivity of 0.05 wt% Zr-doped Fe_2O_3 at various applied potentials, similar to that of bare Fe_2O_3, exhibits a maximum at 1.6 V_{RHE} and decreases at potentials above this (Fig. S14); the optimum potential coincides with that for the bare Fe_2O_3 catalyst. Zr doping improves the ethanol selectivity; the selectivity under 0.05 wt% Zr doping reaches 91 %. The conversion of the 0.05 wt% Zr-doped Fe_2O_3 catalyst is superior to the results of the previous liquid-phase methane–methanol (or ethanol) catalytic conversion (see Table S1). More impressively, the Zr-doped Fe_2O_3 catalyst exhibits high selectivity even at high ethanol production rates (see Fig. S15). We confirm the long–term stability of the electrochemical conversion with the Zr-doped Fe_2O_3 catalyst (Fig. 4g). The 0.05 wt% Zr-doped Fe_2O_3 catalyst exhibits stable operation with only a 10 % reduction in the oxidation current for 18 h. The areal oxidation current values are high compared to those of recent catalysts applied to electrochemical methane conversion (Table S2). After the reaction, the Zr-doped Fe_2O_3 retains the XRD pattern corresponding to α-Fe_2O_3 (Fig. S16). The TEM image exhibits the same size and polyhedral morphology as before the reaction (Fig. S16).

4. Conclusion

We demonstrate electrochemical methane–ethanol conversion by employing Fe_2O_3 catalysts with CO_3^{2-} oxygen source. The free-energy profile for the OER on α-Fe_2O_3 (0001) shows difficulties in maintaining active O* on the catalyst surface due to the second step of the OER (OH* → O*) being the potential determining step. In contrast, the CO_3^{2-} oxygen source generates O* via thermochemical dissociation, ensuring stable formation of O* in a potential range that is not sufficient to promote the OER. We obtain methane conversion productivity that increases with increasing potential in the range of 0.8–1.6 V_{RHE}; however, at higher potentials, the productivity is reduced due to the activation of the OER. The electrochemical methane oxidation on the O–promoted Fe_2O_3 catalyst produces mainly ethanol. DFT calculations show that the ethanol production route consists of O*–induced methane activation, CH_3OH^* deprotonation, and then coupling of CH_2O^* with methane. On

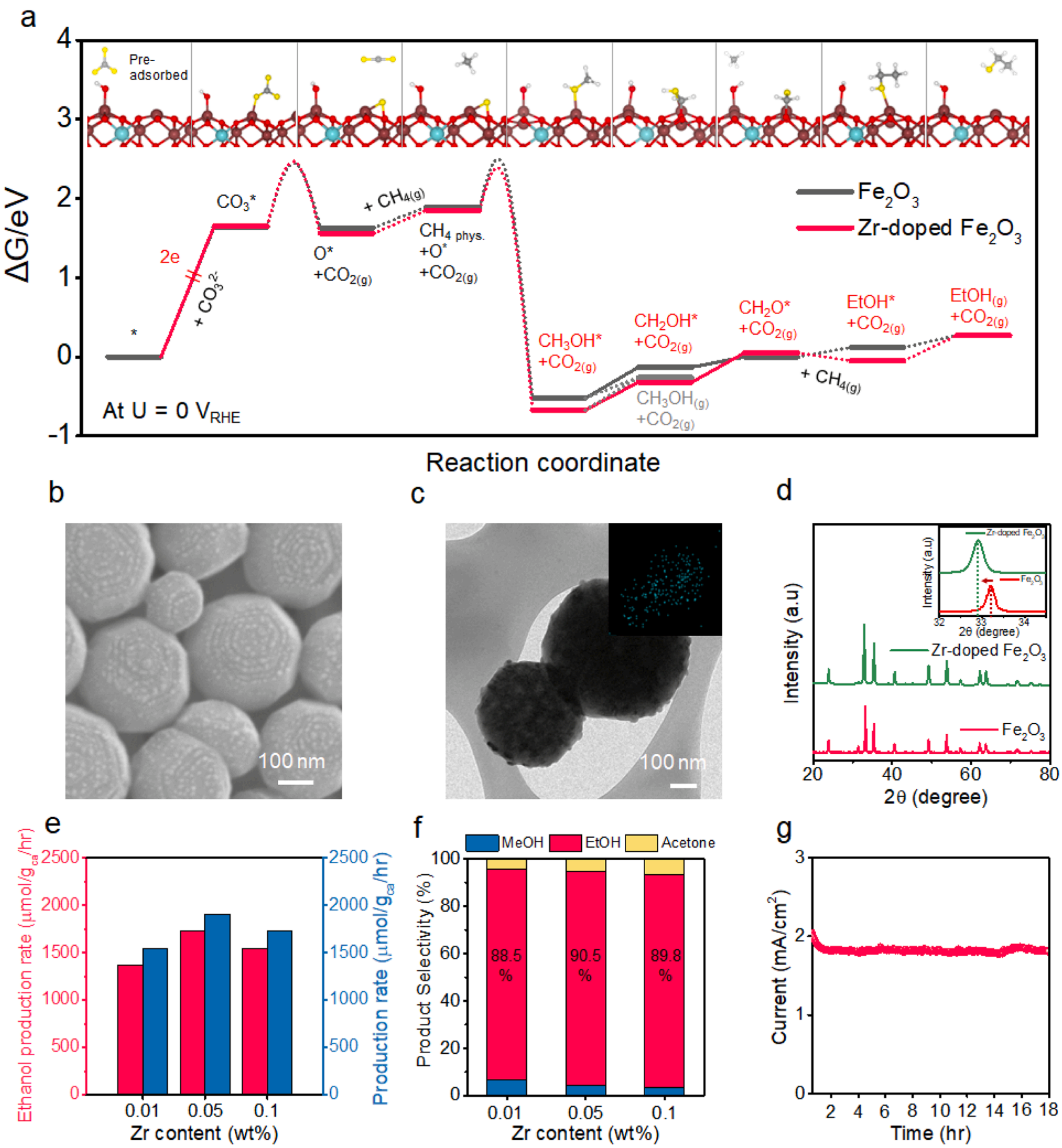

Fig. 4. Effect of Zr doping. (a) Calculated free energy diagrams for O* production and methane–ethanol conversion on the Zr-doped Fe_2O_3 catalyst. The energy profile of Fe_2O_3 is presented for comparison. The cartoons are atomic configurations corresponding to each reaction coordinate. The solid and dashed lines represent the electrochemical and thermochemical steps, respectively. (b) SEM and (c) TEM/EDS images and (d) XRD spectra of the Zr-doped Fe_2O_3 catalyst. The inset of Fig. 4d shows the peaks corresponding to the (104) plane of Zr-doped Fe_2O_3 and Fe_2O_3. (e) Production rates of ethanol and total oxygenates and (f) selectivity for major products with varying Zr content. The applied voltage is 1.6 V_{RHE}. (g) Areal current density at 1.6 V_{RHE} for electrochemical methane oxidation on Zr-doped Fe_2O_3 nanoparticles as a function of reaction time.

the Fe_2O_3 surface, CH_3OH^* deprotonation is thermodynamically preferred to CH_3OH^* desorption, leading to high ethanol selectivity. To further enhance the methane–ethanol conversion, Zr doping is applied. Mechanistic studies show that the Zr dopant allows the formation of OH* that stabilizes only the intermediates that contain the –OH group via hydrogen bonding. We achieve an ethanol production rate of 1198.3 μmol/g_{cat}/hr with a selectivity of 86 % over the Fe_2O_3 catalyst. The 0.05 wt% Zr-doped Fe_2O_3 catalyst achieves a 53 % improvement in the production rate to 1677 μmol/g_{cat}/hr (the total production rate for oxygenates is 1831 μmol/g_{cat}/hr) over bare Fe_2O_3, where the ethanol selectivity is 91 %. The FE for oxygenates on these Fe_2O_3 catalysts reaches 87 %. This achievement with these Fe_2O_3 catalysts with CO_3^{2-} is outstanding compared to the liquid-phase methane–alcohol conversion obtained with various advanced catalysts. Our work presents an understanding and achievement of electrochemical methane conversion under ambient conditions. Moreover, this study sheds light on the direction in which electrochemical catalyst systems are headed for partial oxidation of methane to alcohols.

CRediT authorship contribution statement

Jaehyun Lee: Investigation, Formal analysis, Data curation. **Sung-woo Lee:** Theoretical simulation, Formal analysis, Data curation. **Cheolho Kim:** Data curation. **Jong Suk Yoo:** Conceptualization, Supervision, Writing - original draft, Writing – Review & Editing. **Jun Hyuk Moon**: Conceptualization, Funding acquisition, Supervision, Project administration, Writing - original draft, Writing – Review & Editing.

Declaration of Competing Interest

The authors declare that they have no known competing financial interests or personal relationships that could have appeared to influence the work reported in this paper.

Data Availability

Data will be made available on request.

Acknowledgments

This work was supported by the National Research Foundation of Korea (Grant No. 2021M3D3A1A01022112, 2022R1A2C2005228). The Korea Basic Science Institute is also acknowledged for the XPS measurements. DFT calculations were performed using the computational resources in the Urban Big Data and AI Institute (UBAI) at the University of Seoul, and the Korea Institute of Science and Technology Information (KSC-2021-CRE-0532).

Appendix A. Supporting information

Supplementary data associated with this article can be found in the online version at doi:10.1016/j.apcatb.2023.123633.

References

[1] E.G. Nisbet, E.J. Dlugokencky, P. Bousquet, Methane on the rise—again, Science 343 (2014) 493–495, https://doi.org/10.1126/science.1247828.
[2] D. Saha, H.A. Grappe, A. Chakraborty, G. Orkoulas, Postextraction separation, on-board storage, and catalytic conversion of methane in natural gas: a review, Chem. Rev. 116 (2016) 11436–11499, https://doi.org/10.1021/acs.chemrev.5b00745.
[3] M. Ravi, M. Ranocchiari, J.A. vanBokhoven, The direct catalytic oxidation of methane to methanol—a critical assessment, Angew. Chem. Int. Ed. 56 (2017) 16464–16483, https://doi.org/10.1002/anie.201702550.
[4] Z. Jin, L. Wang, E. Zuidema, K. Mondal, M. Zhang, J. Zhang, C. Wang, X. Meng, H. Yang, C. Mesters, F.-S. Xiao, Hydrophobic zeolite modification for in situ peroxide formation in methane oxidation to methanol, Science 367 (2020) 193–197, https://doi.org/science.aaw1108.
[5] S.J. Blanksby, G.B. Ellison, Bond dissociation energies of organic molecules, Acc. Chem. Res. 36 (2003) 255–263, https://doi.org/10.1021/ar020230d.
[6] A.S. Rosen, J.M. Notestein, R.Q. Snurr, High-valent metal–oxo species at the nodes of metal–triazolate frameworks: the effects of ligand exchange and two-state reactivity for C– H bond activation, Angew. Chem. 132 (2020) 19662–19670, https://doi.org/10.1002/anie.202004458.
[7] Y. Zhou, L. Zhang, W. Wang, Direct functionalization of methane into ethanol over copper modified polymeric carbon nitride via photocatalysis, Nat. Commun. 10 (2019), 506, https://doi.org/10.1038/s41467-019-08454-0.
[8] F. Schüth, Making more from methane, Science 363 (2019) 1282–1283, https://doi.org/10.1126/science.aaw7738.
[9] P. Tang, Q. Zhu, Z. Wu, D. Ma, Methane activation: the past and future, Energy Environ. Sci. 7 (2014) 2580–2591, https://doi.org/10.1039/C4EE00604F.
[10] L.V. Mattos, G. Jacobs, B.H. Davis, F.B. Noronha, Production of hydrogen from ethanol: review of reaction mechanism and catalyst deactivation, Chem. Rev. 112 (2012) 4094–4123, https://doi.org/10.1021/cr2000114.
[11] B.E.R. Snyder, P. Vanelderen, M.L. Bols, S.D. Hallaert, L.H. Böttger, L. Ungur, K. Pierloot, R.A. Schoonheydt, B.F. Sels, E.I. Solomon, The active site of low-temperature methane hydroxylation in iron-containing zeolites, Nature 536 (2016) 317–321, https://doi.org/10.1038/nature19059.
[12] P. Tomkins, M. Ranocchiari, J.A. van Bokhoven, Direct conversion of methane to methanol under mild conditions over Cu-zeolites and beyond, Acc. Chem. Res. 50 (2017) 418–425, https://doi.org/10.1021/acs.accounts.6b00534.
[13] S. Grundner, M.A.C. Markovits, G. Li, M. Tromp, E.A. Pidko, E.J.M. Hensen, A. Jentys, M. Sanchez-Sanchez, J.A. Lercher, Single-site trinuclear copper oxygen clusters in mordenite for selective conversion of methane to methanol, Nat. Commun. 6 (2015), 7546, https://doi.org/10.1038/ncomms8546.
[14] M.H. Mahyuddin, Y. Shiota, K. Yoshizawa, Methane selective oxidation to methanol by metal-exchanged zeolites: a review of active sites and their reactivity, Catal. Sci. Technol. 9 (2019) 1744–1768, https://doi.org/10.1039/C8CY02414F.
[15] M.H. Groothaert, P.J. Smeets, B.F. Sels, P.A. Jacobs, R.A. Schoonheydt, Selective oxidation of methane by the bis(μ-oxo)dicopper core stabilized on ZSM-5 and mordenite zeolites, J. Am. Chem. Soc. 127 (2005) 1394–1395, https://doi.org/10.1021/ja047158u.
[16] J. Xu, R.D. Armstrong, G. Shaw, N.F. Dummer, S.J. Freakley, S.H. Taylor, G. J. Hutchings, Continuous selective oxidation of methane to methanol over Cu- and Fe-modified ZSM-5 catalysts in a flow reactor, Catal. Today 270 (2016) 93–100, https://doi.org/10.1016/j.cattod.2015.09.011.
[17] S. Yuan, Y. Li, J. Peng, Y.M. Questell-Santiago, K. Akkiraju, L. Giordano, D. J. Zheng, S. Bagi, Y. Román-Leshkov, Y. Shao-Horn, Conversion of methane into liquid fuels—bridging thermal catalysis with electrocatalysis, Adv. Energy Mater. 10 (2020), 2002154, https://doi.org/10.1002/aenm.202002154.
[18] A.H. Bagherzadeh Mostaghimi, T.A. Al-Attas, M.G. Kibria, S. Siahrostami, A review on electrocatalytic oxidation of methane to oxygenates, J. Mater. Chem. A 8 (2020) 15575–15590, https://doi.org/10.1039/D0TA03758C.
[19] L. Arnarson, P.S. Schmidt, M. Pandey, A. Bagger, K.S. Thygesen, I.E.L. Stephens, J. Rossmeisl, Fundamental limitation of electrocatalytic methane conversion to methanol, Phys. Chem. Chem. Phys. 20 (2018) 11152–11159, https://doi.org/10.1039/C8CP01476K.
[20] Y. Kang, Z. Li, X. Lv, W. Song, Y. Wei, X. Zhang, J. Liu, Z. Zhao, Active oxygen promoted electrochemical conversion of methane on two-dimensional carbide (MXenes): from stability, reactivity and selectivity, J. Catal. 393 (2021) 20–29, https://doi.org/10.1016/j.jcat.2020.11.008.
[21] X. Meng, X. Cui, N.P. Rajan, L. Yu, D. Deng, X. Bao, Direct methane conversion under mild condition by thermo-, electro-, or photocatalysis, Chem 5 (2019) 2296–2325, https://doi.org/10.1016/j.chempr.2019.05.008.
[22] S.J. Freakley, N. Dimitratos, D.J. Willock, S.H. Taylor, C.J. Kiely, G.J. Hutchings, Methane oxidation to methanol in water, Acc. Chem. Res. 54 (2021) 2614–2623, https://doi.org/10.1021/acs.accounts.1c00129.
[23] Z. Liu, E. Huang, I. Orozco, W. Liao, R.M. Palomino, N. Rui, T. Duchoň, S. Nemšák, D.C. Grinter, M. Mahapatra, P. Liu, J.A. Rodriguez, S.D. Senanayake, Water-promoted interfacial pathways in methane oxidation to methanol on a CeO2-Cu2O catalyst, Science 368 (2020) 513–517, https://doi.org/10.1126/science.aba5005.
[24] A. Prajapati, A. Collins Brianna, D. Goodpaster Jason, R. Singh Meenesh, Fundamental insight into electrochemical oxidation of methane towards methanol on transition metal oxides, Proc. Natl. Acad. Sci. 118 (2021), e2023233118, https://doi.org/10.1073/pnas.2023233118.
[25] Z. Xie, M. Chen, Y. Chen, A. Guan, Q. Han, G. Zheng, Electrocatalytic methane oxidation to ethanol via Rh/ZnO nanosheets, J. Phys. Chem. C. 125 (2021) 13324–13330, https://doi.org/10.1021/acs.jpcc.1c03416.
[26] Y. Song, Y. Zhao, G. Nan, W. Chen, Z. Guo, S. Li, Z. Tang, W. Wei, Y. Sun, Electrocatalytic oxidation of methane to ethanol via NiO/Ni interface, Appl. Catal. B 270 (2020), 118888, https://doi.org/10.1016/j.apcatb.2020.118888.
[27] M. Chen, X. Lv, A. Guan, C. Peng, L. Qian, G. Zheng, Electrocatalytic methane oxidation to formate on magnesium based metal-organic frameworks, J. Colloid Interface Sci. 623 (2022) 348–353, https://doi.org/10.1016/j.jcis.2022.05.060.
[28] Y. Kang, M. Tian, C. Huang, J. Lin, B. Hou, X. Pan, L. Li, A.I. Rykov, J. Wang, X. Wang, Improving syngas selectivity of Fe2O3/Al2O3 with yttrium modification in chemical looping methane conversion, ACS Catal. 9 (2019) 8373–8382, https://doi.org/10.1021/acscatal.9b02730.
[29] P. Sharma, J.-W. Jang, J.S. Lee, Key strategies to advance the photoelectrochemical water splitting performance of α-Fe2O3 photoanode, ChemCatChem 11 (2019) 157–179, https://doi.org/10.1002/cctc.201801187.
[30] N. Spinner, W.E. Mustain, Electrochemical methane activation and conversion to oxygenates at room temperature, J. Electrochem. Soc. 160 (2013) F1275, https://doi.org/10.1149/2.071311jes.
[31] T.J. Omasta, W.A. Rigdon, C.A. Lewis, R.J. Stanis, R. Liu, C.Q. Fan, W.E. Mustain, Two pathways for near room temperature electrochemical conversion of methane to methanol, ECS Trans. 66 (2015) 129, https://doi.org/10.1149/06608.0129ecst.
[32] S.-W. Cao, Y.-J. Zhu, Monodisperse α-Fe2O3 mesoporous microspheres: one-step NaCl-assisted microwave-solvothermal preparation, size control and photocatalytic property, Nanoscale Res Lett. 6 (2010) 1, https://doi.org/10.1007/s11671-010-9742-7.
[33] S. Foraita, J.L. Fulton, Z.A. Chase, A. Vjunov, P. Xu, E. Baráth, D.M. Camaioni, C. Zhao, J.A. Lercher, Impact of the oxygen defects and the hydrogen concentration on the surface of tetragonal and monoclinic ZrO2 on the reduction rates of stearic acid on Ni/ZrO2, Chem. -Eur. J. 21 (2015) 2423–2434, https://doi.org/10.1002/chem.201405312.
[34] N. Yatom, O. Neufeld, M. Caspary Toroker, Toward settling the debate on the role of Fe2O3 surface states for water splitting, J. Phys. Chem. C 119 (2015) 24789–24795, https://doi.org/10.1021/acs.jpcc.5b06128.
[35] H. Hajiyani, R. Pentcheva, Influence of 3d, 4d, and 5d dopants on the oxygen evolution reaction at α-Fe2O3(0001) under dark and illumination conditions, J. Chem. Phys. 152 (2020), 124709, https://doi.org/10.1063/1.5143236.
[36] Z. Wang, X. Guo, J. Montoya, J.K. Nørskov, Predicting aqueous stability of solid with computed Pourbaix diagram using SCAN functional, Npj Comput. Mater. 6 (2020), 160, https://doi.org/10.1038/s41524-020-00430-3.
[37] J. Barthel, R. Deiss, The limits of the Pourbaix diagram in the interpretation of the kinetics of corrosion and cathodic protection of underground pipelines, Mater. Corros. 72 (2021) 434–445, https://doi.org/10.1002/maco.202011977.

[38] S. Arya Gopal, A. Edathiparambil Poulose, C. Sudakar, A. Muthukrishnan, Kinetic insights into the mechanism of oxygen reduction reaction on Fe2O3/C composites, ACS Appl. Mater. Interfaces 13 (2021) 44195–44206, https://doi.org/10.1021/acsami.1c10114.

[39] J. Lee, J. Yang, J.H. Moon, Solar cell-powered electrochemical methane-to-methanol conversion with CuO/CeO2 catalysts, ACS Energy Lett. 6 (2021) 893–899, https://doi.org/10.1021/acsenergylett.0c02553.

[40] M. Ma, C. Oh, J. Kim, J.H. Moon, J.H. Park, Electrochemical CH4 oxidation into acids and ketones on ZrO2:NiCo2O4 quasi-solid solution nanowire catalyst, Appl. Catal. B 259 (2019), 118095, https://doi.org/10.1016/j.apcatb.2019.118095.

[41] L. Chen, X. Liang, X. Li, J. Pei, H. Lin, D. Jia, W. Chen, D. Wang, Y. Li, Promoting electrocatalytic methanol oxidation of platinum nanoparticles by cerium modification, Nano Energy 73 (2020), 104784, https://doi.org/10.1016/j.nanoen.2020.104784.

[42] M. Li, Z. Zhao, W. Zhang, M. Luo, L. Tao, Y. Sun, Z. Xia, Y. Chao, K. Yin, Q. Zhang, L. Gu, W. Yang, Y. Yu, G. Lu, S. Guo, Sub-monolayer YOx/MoOx on ultrathin Pt nanowires boosts alcohol oxidation electrocatalysis, Adv. Mater. 33 (2021), 2103762, https://doi.org/10.1002/adma.202103762.

[43] L. Chen, X. Liang, D. Wang, Z. Yang, C.-T. He, W. Zhao, J. Pei, Y. Xue, Platinum–ruthenium single atom alloy as a bifunctional electrocatalyst toward methanol and hydrogen oxidation reactions, ACS Appl. Mater. Interfaces 14 (2022) 27814–27822, https://doi.org/10.1021/acsami.2c02905.

[44] T. Clarys, T. Stuyver, F. De Proft, P. Geerlings, Extending conceptual DFT to include additional variables: oriented external electric field, Phys. Chem. Chem. Phys. 23 (2021) 990–1005, https://doi.org/10.1039/D0CP05277A.

[45] V.O.O. Gonçalves, P.M. de Souza, T. Cabioc'h, V.T. da Silva, F.B. Noronha, F. Richard, Hydrodeoxygenation of m-cresol over nickel and nickel phosphide based catalysts. Influence of the nature of the active phase and the support, Appl. Catal. B 219 (2017) 619–628, https://doi.org/10.1016/j.apcatb.2017.07.042.

[46] E. Iype, S.V. Nedea, C.C.M. Rindt, A.A. van Steenhoven, H.A. Zondag, A.P. J. Jansen, DFT study on characterization of hydrogen bonds in the hydrates of MgSO4, J. Phys. Chem. C. 116 (2012) 18584–18590, https://doi.org/10.1021/jp3025649.

[47] W. Hujo, S. Grimme, Comparison of the performance of dispersion-corrected density functional theory for weak hydrogen bonds, Phys. Chem. Chem. Phys. 13 (2011) 13942–13950, https://doi.org/10.1039/C1CP20591A.

[48] G.A. DiLabio, E.R. Johnson, A. Otero-de-la-Roza, Performance of conventional and dispersion-corrected density-functional theory methods for hydrogen bonding interaction energies, Phys. Chem. Chem. Phys. 15 (2013) 12821–12828, https://doi.org/10.1039/C3CP51559A.